Supporting Information for

Monitoring Morphological Changes in 2D Monolayer Semiconductors Using Atom-Thick Plasmonic Nanocavities

*Daniel O. Sigle,[1] Jan Mertens,[1] Lars O. Herrmann,[1] Richard W. Bowman,[1] Sandrine Ithurria,[2] Benoit Dubertret,[2] Yumeng Shi,[3] Hui Ying Yang,[3] Christos Tserkezis,[4] Javier Aizpurua,[4] Jeremy J. Baumberg[1]**

* jjb12@cam.ac.uk

[1]NanoPhotonics Centre, Cavendish Laboratory, University of Cambridge, Cambridge, CB3 0HE, United Kingdom

[2]Laboratoire de Physique et d'Etude des Matériaux, UMR8213 du CNRS, 10 rue Vauquelin 75231 Paris, France

[3]Pillar of Engineering Product Development, Singapore University of Technology and Design, Singapore 138682, Singapore

[4]Center for Materials Physics, CSIC-UPV/EHU and DIPC, Paseo Manuel de Lardizabal 5, 20018 Donostia-San Sebastian, Spain

A) AFM of CdSe and MoS_2 films on Au planar surfaces

In the samples prepared on Au, the MoS_2 monolayer crystals cover ~50% of the gold surface. Similarly, the CdSe platelets form a monolayer with a surface coverage of ~60% (Fig. S1).

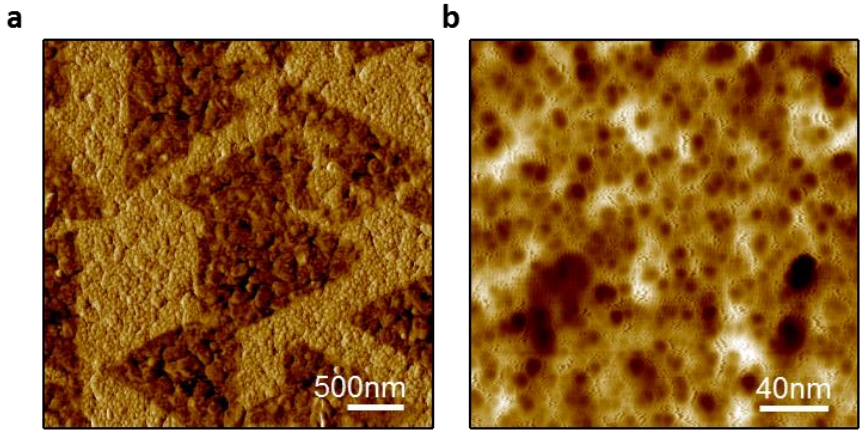

Figure S1 | a, Phase contrast image of MoS_2 crystals deposited on Au surface. **b,** Amplitude contrast image of CdSe platelet film on Au surface. Inset shows a 100nm AuNP on the surface.

B) SERS of MoS_2 and CdSe in the NPoM geometry

In order to ensure that the nanoparticles are placed directly on top of the semiconductor layers, we compare the Raman scattering of the CdSe and MoS_2 spacer without nanoparticles and in the NPoM geometry. We employ excitation wavelengths of 532nm for the CdSe and 633nm for the MoS_2 and 1mW optical power. Both wavelengths lead to significant plasmonic activity in the plasmonic MIM-waveguide nanocavity and enable excitation near the bandgap of the respective material, leading to resonant Raman effects. The strongly enhanced SERS observed clearly demonstrates that the AuNPs are on top of the semiconductor layers and that they do not introduce significant strain or doping.

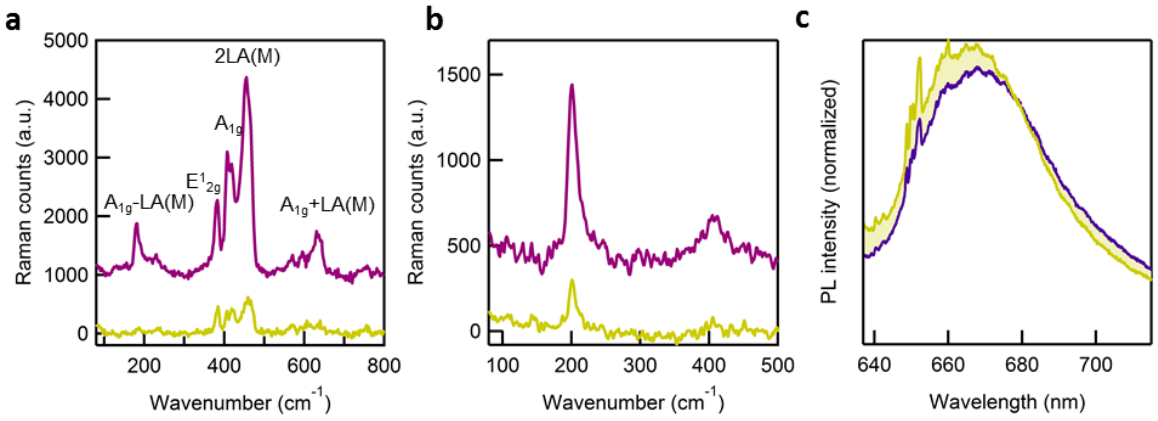

Figure S2 | Raman spectra on Au surface with NP (purple) and without NP (yellow) showing SERS in the NPoM geometry for 633nm excitation. **a**, MoS_2 and **b**, CdSe. Note backgrounds are subtracted and offset for clarity. **c,** Photoluminescence of MoS_2 before (yellow) and after 6min (purple) of irradiation with UV laser light on a single NPoM.

Both spacer materials exhibit clearly enhanced Raman scattering when placed into the NPoM geometry compared to spectra taken on a flat Au surface covered by the semiconductor layers (Fig. S2). In the case of the MoS_2 spacer, the Raman scattering amplitude is amplified by a factor of ~10. We note that this overall enhancement actually stems from only the tiny field-enhanced volume in the gap whose lateral diameter is given by $w = \sqrt{Rd}$ (R nanosphere radius, d gap distance).[1] Taking into account that the collection area diameter is ~1μm, we estimate a SERS-enhancement in the junction of $>10^5$.

In the case of the CdSe spacer, the observed enhancement is approximately a factor of 10 lower due to the less intense plasmon field at 532nm. While absence of NPs only allows observation of the $(LO)_1$ phonon near 200cm^{-1}, the nanogap environment additionally reveals the first overtone $2(LO)_1$ near 400cm^{-1}.

The photoluminescence of MoS_2 is virtually unaffected by UV laser irradiation (Fig. S2c). This shows that the MoS_2 remains entirely intact during the experiments and does not

undergo photodecomposition at the optical densities used in our experiments. Slight variations of the Raman line strengths are a result of the changes in field enhancement and orientation as the nanoparticle facet grows.

C) Polarisation of the dipole far-field scattering.

In order to fully confirm the plasmonic nature of the dipolar infrared mode, we investigated the polarisation of its far-field radiation (Fig. S3a). A λ/2-plate was placed in the scattered beam while the incident supercontinuum light was unpolarised. The intensity of the scattered light shows a clear dependence on the analyser position as expected. The spectral position of the dipolar mode is highly sensitive to the initial facet size of the NP but in all NPoMs is located between 1100nm and 1200nm with good reproducibility (Fig. S3b).

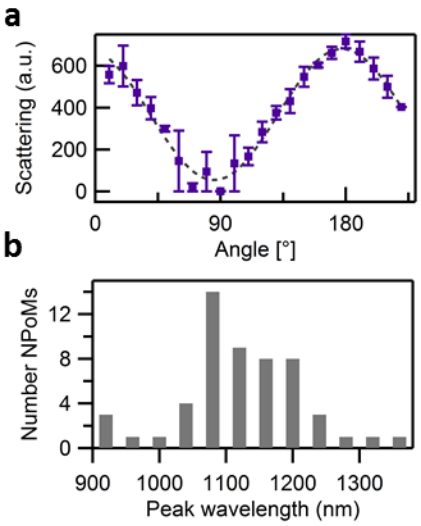

Figure S3 | a, Angle-dependence of the dipolar infrared mode intensity. At 0° and 180°, the vertically polarised field is transmitted **b,** Peak wavelength of the ***D*** infrared mode for a range of individual NPoMs.

D) DF scattering of NPoM without semiconductor spacer

Omitting the semiconductor spacer leads to conducting contact of the AuNP with the surface. A charge oscillation across nanoparticle and image charge is present, leading to only a single coupled mode (as seen in the typical spectra of Fig. S4 observed on many NPoMs). As the charge separation between the AuNP and the image is suppressed, no mode splitting can be observed in contrast to the semiconductor-spaced NPoM.

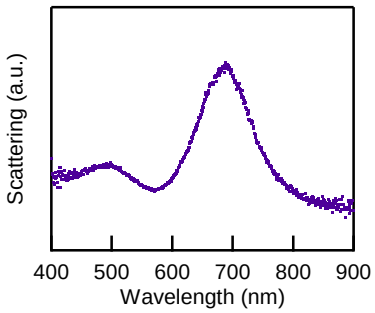

Figure S4 | Single longitudinal resonance seen for Au NPoM on gold surface without any spacer.

E) Photoluminescence decay and phonon shift

We investigate the kinetics of the photoluminescence (PL) decay and the phonon shifts on CdSe platelets in the NPoM geometry using a Renishaw inVia Raman microscope with multiple excitation sources.

Using a 488nm excitation laser, we record the photoluminescence amplitude over time. Although the PL spectral peak does not shift in energy, it decays following a double exponential function and always stabilizes at 15%-30% of the initial amplitude, depending on the irradiation power (Fig. S5a,b). Since power levels even higher than those applied in the DF-irradiation experiments do not lead to a complete PL drop, we exclude the possibility of complete CdSe ablation.

The optical phonons in the CdSe platelets are further investigated using 532nm excitation. The Raman scattering peak intensity of the CdSe $(LO)_1$ phonon decays along with the photoluminescence, but also a significant fraction remains visible even after long irradiation times. We note a spectral shift from 201cm^{-1} to 208cm^{-1} after irradiating with the blue laser for 30 seconds (Fig. S4c). Such phonon shifts are known in core-shell type quantum dots[2] and are generally attributed to increased strain in the crystal as a result of a lattice mismatch between core and shell.

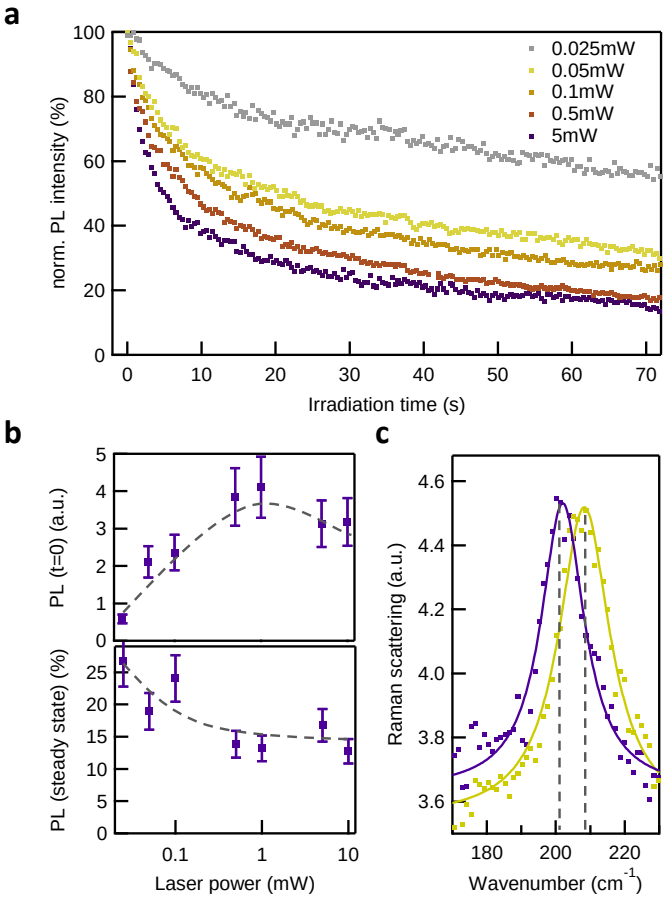

Figure S5 | a, CdSe Photoluminescence amplitude over time for different irradiation levels (normalized at t=0). **b,** Top: Initial PL amplitude for different optical powers; bottom: PL steady state intensity as a fraction of initial amplitude. **c,** $(LO)_1$ phonon of the CdSe platelet before (purple) and after (yellow) 30s irradiation with 1mW. The peak shifts from 201cm^{-1} to 208cm^{-1}.

F) Photochemistry

The photochemistry of CdSe is well known in a variety of configurations, and we summarise how this relates to the current observations. We suggest a photoinduced transformation of the CdSe surface monolayer according to the scheme[3]

$$CdSe + 2h^{+} \rightarrow Cd^{2+} + Se.$$

As a result of the light-induced separation of electron-hole pairs at the interfaces, the CdSe is converted into atomic Se and Cd^{2+} ions. The Cd ions further react with environmental water to $Cd(OH)_2$ and thence further to CdO. Evidence for this is the observed phonon shift described in section (E). Further we note the occurrence of a CdO Raman peak near 270cm^{-1}. Once the top layer of the platelet has reacted, it acts as a protective layer preventing further oxidation.

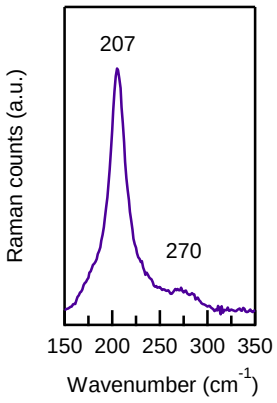

Figure S6 | Raman scattering of CdSe platelets after irradiation with 448nm light.

G) Theory: MIM waveguide model

The dispersion relation of metal-insulator-metal waveguides with a gap d, is given by the solution of [4]

$$\tanh\left(\frac{\beta_d d}{2}\right) = -\frac{\varepsilon_d \beta_m}{\varepsilon_m \beta_d}$$

where $\beta_{m,d} = \sqrt{k_\parallel^2 - \varepsilon_{m,d} k_0^2}$. For the extremely small gaps used here, this expression can be accurately approximated. The MIM waveguide dispersion $E(k_\parallel)$, can be calculated[4,5] for very thin gaps, $d < 10$nm, from

$$\left(\frac{k_\parallel}{E/\hbar c}\right)^2 = \varepsilon_d + \frac{\gamma}{2}\left[1 + \sqrt{1 + 4(\varepsilon_d - \varepsilon_m)/\gamma}\right] \qquad \text{Eqn (S.1)}$$

where $\gamma = \left(\frac{-2\hbar c\, \varepsilon_d}{E\, d\, \varepsilon_m}\right)^2$, for dielectric constants of ε_m (ε_d) in the metal (gap dielectric). The dispersion relation is plotted in Fig. S7 for the typical SPP on flat Au (black dashed) and the gap plasmon in a d=0.6nm gap, with ε_d=1.63 (typical of the monolayer semiconductors).

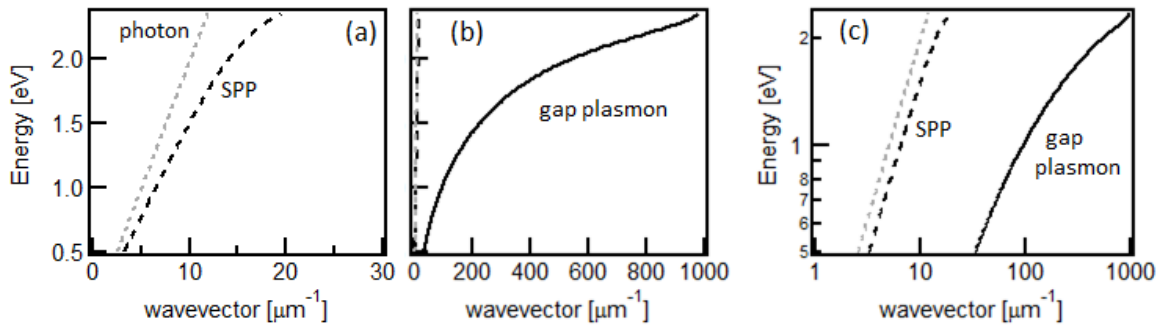

Figure S7 | Dispersion relation comparing SPP on a single Au surface with the gap plasmon between two Au mirrors spaced 0.6nm apart, and filled with *n*=1.27.

This yields an effective refractive index which is very sensitive to the gap size, and the dielectric filling (Fig. S8).

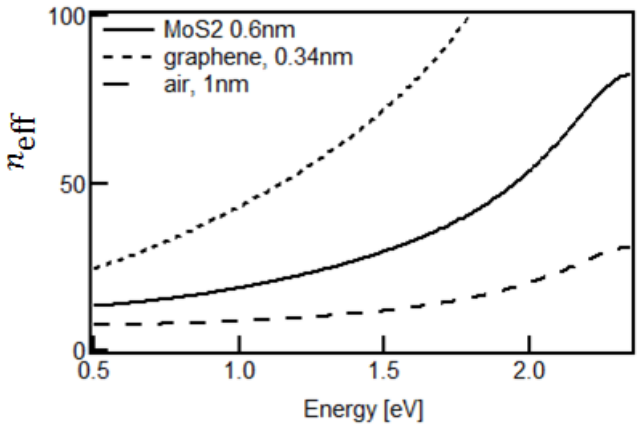

Figure S8 | Effective refractive index for gap plasmons with different gaps and different spacer materials.

While a full simulation is needed to find the exact spectral position of the resonant modes which reflect between the discontinuities at either end of this plasmonic MIM waveguide, simple indications can be extracted from this model. We assume perfect reflection at each end, due to the strong mismatch in impedance within and outside the MIM plasmon waveguide. In practise the phase shift on reflection and the reflectivity of the plasmon depend sensitively on the exact morphology at the facet edges (and this is likely seen in the experiments). However full simulations show that the field strays little outside the facet area for such narrow gaps, and hence this is a reasonable assumption. By using this boundary condition on a circular rim, we find the mode quantisation as given in the main text. We solve simply using Equation (S1) to extract n_{eff} and use this to find the precise wavelengths. An even simpler solution results for the small gap situation, in which $\gamma \gg \varepsilon_m, \varepsilon_d$ so that

$$n_{\mathrm{eff}} = -\frac{2\varepsilon_d}{d\varepsilon_m k_0}.$$

Together with $\lambda_i = \pi w\, n_{\mathrm{eff}}/\alpha_i$, this leads to

$$\varepsilon_m(\lambda_i) = -\frac{w\varepsilon_d}{d\alpha_i}$$

which can be simply solved to find the set of modes, λ_i. Simplifying even further, the Drude model which works well for λ>550nm can be used to approximate the metal dielectric constant, giving Equation (1) in the main text.

This model is also sufficient to consider the tuning of the different modes as the facet width increases in time ($\dot{w}$), giving

$$\dot{\lambda}_i = \frac{\partial \lambda_i}{\partial w} \cdot \frac{\partial w}{\partial t} = \frac{\varepsilon_d \lambda_p^2}{2d\alpha_i \lambda_i} \quad \dot{w}$$

This allows the ratio of the tuning rates of the different lines to be extracted, so $\dot{\lambda}_3/\dot{\lambda}_5 = \alpha_5\lambda_5/\alpha_3\lambda_3$ ~1.4, which matches the experimental observations. We can also use this formula to estimate the number of atoms arriving at the edge of the facet, $dN = \pi w dw/a^2$, giving the formula for $\dot{N}$ in the main text.

H) Effect of electron microscopy on the optical NPoM scattering

The optical scattering of NPoMs is investigated before and after imaging in a scanning electron microscope (SEM) (Fig. S9).

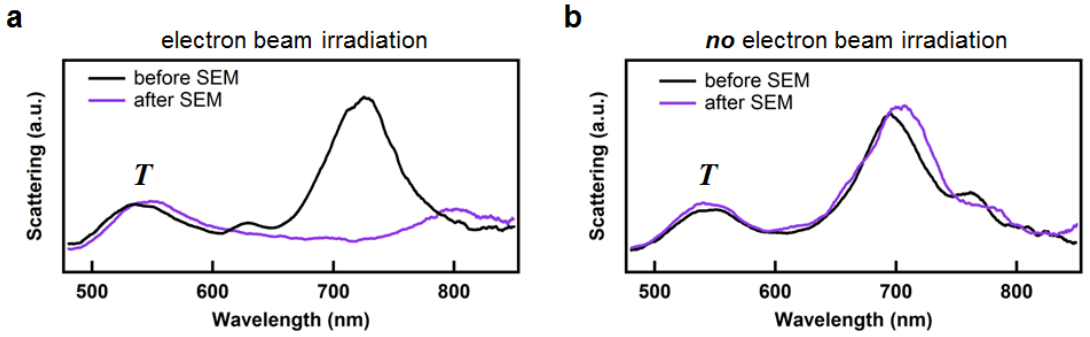

Figure S9 | a, Scattering spectra of AuNP before (black) and after (purple) SEM examination. **b,** Control measurement: scattering spectra of a NP on the same sample that has

not been irradiated with the electron beam before (black) and after (purple) the sample has been in the SEM.

The electron beam exposure completely changes the optical scattering spectrum (Fig. S9a) while scattering from a particle on the same sample that has not been directly irradiated with the electron beam remains unchanged (Fig. S9b). As always seen in electron microscopy, carbon contamination is deposited in the scanning area of the beam[6,7], affecting the scattering spectrum but also the Au adatom mobility. Interrogation with an electron beam hence introduces irreversible changes into the system which prevents direct structural detection of such laser-induced morphological changes.[8]

I) Thermal activation of plasmon tuning

As well as using optical irradiation, we find thermally-activated changes in the NPoM scattering when heating the samples and simultaneously recording the scattering spectra (Fig. S10). In these experiments the AuNP and Au surface are instead spaced apart by a thin insulating ligand layer.

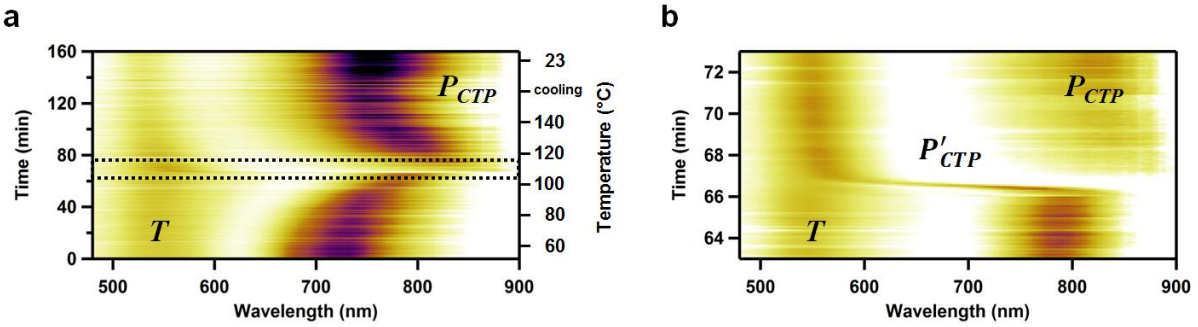

Figure S10 | Scattering spectra of a AuNP on heated Au substrate. **a,** Changes in scattering vs time, temperature and wavelength. The dashed region is magnified in **b** where the substrate is near 100°C.

Heating of the substrates is performed on a heating stage mounted on the microscope in 10°C steps with a rate of $10^{°C}/_{min}$ and after each heating step the temperature is kept constant for 10min. Once heated above 60°C, redshifts of the coupled plasmonic mode are observed similar as discussed in the main paper, while the T-mode is little affected. We conclude that thermal energy also leads to increased atomic mobility in the AuNPs and an increasing facet size. Heating the sample above 100°C leads to sudden blueshifts of the modes from the IR as the AuNP and surface fuse together forming charge transfer plasmons (P_{CTP}, P'_{CTP}) (Fig. S10b) with increasing conductivity.[9–12] The P'_{CTP} mode shifts rapidly from the IR towards the blue at ~$6^{nm}/_{s}$ and merges into the T-mode. A slower shift is observed for the P_{CTP} mode which reaches an equilibrium state at a wavelength of ~750nm. This proves that Au atom migration can occur, leading in this case to conductive contact with the substrate, which is not possible with the impermeable inorganic semiconductor platelets.

J) Cross-sectional NPoM imaging with DF-STEM

To investigate the contact area of the facetted AuNP with the surface underneath, we use dark-field scanning transmission electron microscopy (DF-STEM) for cross-sectional imaging of the NPoM construct which is sectioned by focussed ion beam milling at the position of a single nanoparticle. The sample fabrication process is illustrated in Fig. S11.

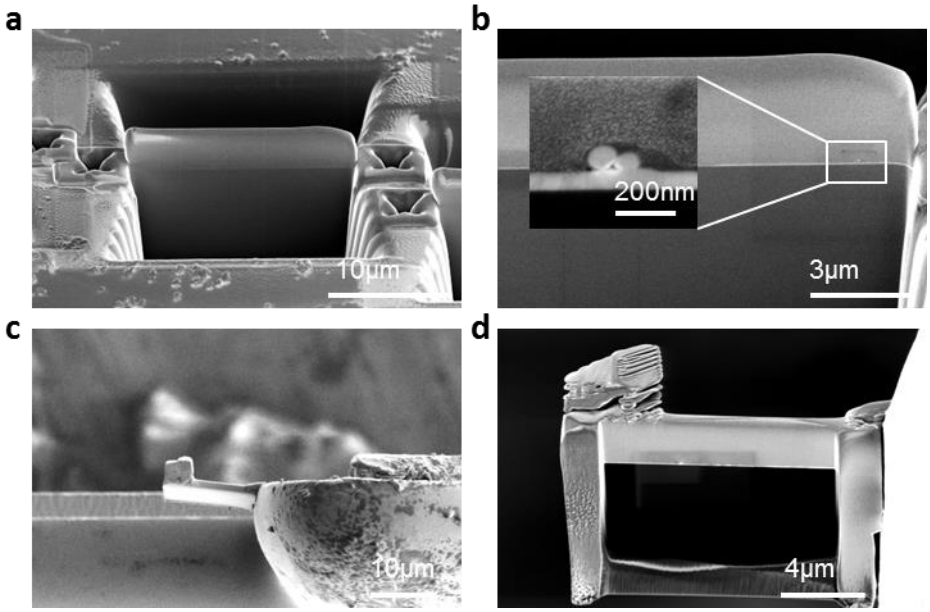

Figure S11 | a, b, FIB is applied to isolate a cross-sectional slice through the sample after evaporating a Pt matrix from the top. Inset in **b** shows two AuNP embedded in the slab. **c,d** The slice is mounted on a TEM grid by evaporating a thin Pt layer.

First, a NPoM is embedded in a platinum (Pt) matrix which is evaporated onto the sample surface. Focussed ion beam milling (FIB) is used to isolate a cross-sectional slice from the sample, which is then mounted on a TEM grid with a nanomanipulator *via* local deposition of a Pt layer at the touching points. The slice is further thinned to a thickness of ~100nm using FIB and finally imaged *via* DF-STEM in a Hitachi S-5500 at 30kV acceleration voltage.[13]

While the facet and the formation of the MIM-cavity with the surface is clearly seen (Fig. 1 in the manuscript), the atom migration in the gap cannot be resolved. The imaging technique is highly invasive due to the deposition of the Pt matrix as well as carbon contamination, preventing the same nanoparticle being imaged before and after optical irradiation.

References:

(1) Savage, K. J.; Hawkeye, M. M.; Esteban, R.; Borisov, A. G.; Aizpurua, J.; Baumberg, J. J. Revealing the Quantum Regime in Tunnelling Plasmonics. *Nature* **2012**, *491*, 574–577.

(2) Lu, L.; Xu, X.-L.; Liang, W.-T.; Lu, H.-F. Raman Analysis of CdSe/CdS Core-Shell Quantum Dots with Different CdS Shell Thickness. *J. Phys. Condens. Matter* **2007**, *19*, 406221.

(3) Aldana, J.; Wang, Y. a; Peng, X. Photochemical Instability of CdSe Nanocrystals Coated by Hydrophilic Thiols. *J. Am. Chem. Soc.* **2001**, *123*, 8844–8850.

(4) Kuttge, M.; Cai, W.; García de Abajo, F.; Polman, A. Dispersion of Metal-Insulator-Metal Plasmon Polaritons Probed by Cathodoluminescence Imaging Spectroscopy. *Phys. Rev. B* **2009**, *80*, 033409.

(5) Bozhevolnyi, S. I.; Søndergaard, T. General Properties of Slow-Plasmon Resonant Nanostructures: Nano-Antennas and Resonators. *Opt. Express* **2007**, *15*, 10869–10877.

(6) Egerton, R. F.; Li, P.; Malac, M. Radiation Damage in the TEM and SEM. *Micron* **2004**, *35*, 399–409.

(7) Horiuchi, S.; Hanada, T.; Ebisawa, M.; Matsuda, Y.; Kobayashi, M. Contamination-Free Transmission Electron Microscopy for High-Resolution. *ACS Nano* **2009**, *3*, 1297–1304.

(8) Hobbs, L. W. Electron-Beam Sensitivity in Inorganic Specimens. *Ultramicroscopy* **1987**, *23*, 339–344.

(9) Atay, T.; Song, J.-H.; Nurmikko, A. V. Strongly Interacting Plasmon Nanoparticle Pairs: From Dipole−Dipole Interaction to Conductively Coupled Regime. *Nano Lett.* **2004**, *4*, 1627–1631.

(10) Romero, I.; Aizpurua, J.; Bryant, G. W.; Garcia de Abajo, F. J. Plasmons in Nearly Touching Metallic Nanoparticles: Singular Response in the Limit of Touching Dimers. *Opt. Express* **2006**, *14*, 9988–9999.

(11) Esteban, R.; Borisov, A. G.; Nordlander, P.; Aizpurua, J. Bridging Quantum and Classical Plasmonics with a Quantum-Corrected Model. *Nat. Commun.* **2012**, *3*, 825.

(12) Scholl, J. a; García-Etxarri, A.; Koh, A. L.; Dionne, J. a. Observation of Quantum Tunneling between Two Plasmonic Nanoparticles. *Nano Lett.* **2013**, *13*, 564–569.

(13) Mubeen, S.; Zhang, S.; Kim, N.; Lee, S.; Krämer, S.; Xu, H.; Moskovits, M. Plasmonic Properties of Gold Nanoparticles Separated from a Gold Mirror by an Ultrathin Oxide. *Nano Lett.* **2012**, *12*, 2088–2094.